UC Berkeley
SEMM Reports Series

Title

Cyclic steady states of nonlinear electro-mechanical devices

Permalink

https://escholarship.org/uc/item/5dv7j12x

Authors

Brandsetter, Gerd

Govindjee, Sanjay

Publication Date

2016-06-01

Report No. UCB/SEMM-2016/01	Structural Engineering Mechanics and Materials

Cyclic steady states of nonlinear electro-mechanical devices

By

Gerd Brandstetter and Sanjay Govindjee

June 2016	Department of Civil and Environmental Engineering University of California, Berkeley

Cyclic steady states of nonlinear electro-mechanical devices excited at resonance

G. Brandstetter[*]and S. Govindjee[†‡]

June 24, 2016

Abstract

We present an efficient numerical method to solve for cyclic steady states of nonlinear electro-mechanical devices excited at resonance. Many electro-mechanical systems are designed to operate at resonance, where the ramp-up simulation to steady state is computationally very expensive – especially when low damping is present. The proposed method relies on a Newton-Krylov shooting scheme for the direct calculation of the cyclic steady state, as opposed to a naïve transient time-stepping from zero initial conditions. We use a recently developed high-order Eulerian-Lagrangian finite element method in combination with an energy-preserving dynamic contact algorithm in order to solve the coupled electro-mechanical boundary value problem. The nonlinear coupled equations are evolved by means of an operator split of the mechanical and electrical problem with an explicit as well as implicit approach. The presented benchmark examples include the first three fundamental modes of a vibrating nanotube, as well as a micro-electro-mechanical disk resonator in dynamic steady contact. For the examples discussed, we observe power law computational speed-ups of the form $S = 0.6 \cdot \xi^{-0.8}$, where ξ is the linear damping ratio of the corresponding resonance frequency.

---

[*]University of California, Berkeley, CA

[†]University of California, Berkeley, CA

[‡]E-mail: s_g at berkeley dot edu

1

1   Introduction

In today's micro-electro-mechanical systems / nano-electro-mechanical systems (MEMS / NEMS), many components are designed to operate at resonance. As particular examples, we mention the recent micro-mechanical resonant switch (reso-switch) by [1], and the nanotube radio by [2]. Other examples include MEMS resonators or the electro-mechanical charge pump as in [3, 4] and references therein. Such devices show great potential to improve upon their semiconductor-based counterparts which require unconventional and expensive transistors.

For the resonant systems discussed in this work, one is typically interested in simulating the operating mode at steady state. In order to find the steady state solution, one traditionally evolves the time-dependant electro-mechanical equations from typically zero initial conditions until a steady state is reached. The number of cycles to reach a steady state by such naïve time stepping may be many thousands or even millions, depending on the damping of the system. Especially for modern designs with very low damping, the simulation up to a steady state will become very expensive, or may be even impossible with this classical approach. In this work we address an alternative, more efficient method to find cyclic steady states directly (CSS method). The CSS method has been inspired by recent works [5, 6], where a cyclic steady state is calculated directly by means of a Newton-Krylov shooting scheme. In [6], the authors consider the evolution of treaded rolling bodies. Other works on Couette turbulence [7], integrable equations [8], mode-locked lasers [9], or surface water waves [10] have used a similar mathematical framework. To our knowledge, we demonstrate for the first time the application of the CSS method in the context of electro-mechanical systems, and in the presence of highly nonlinear shock-like response due to electro-mechanical impact. As will be observed, the CSS method shows strong speed-ups in comparison to traditional time stepping, and opens completely new areas for the simulation of electro-mechanical systems in the face of very low damping.

We note that the simulation of the electro-mechanical systems in this work present further challenges that have been addressed in separate work [11, 12, 13]: the coupled simulation of the electro-mechanical equations by itself, the solution of the electrical field in the entire space, and nonlinear deformation involving shock-like response due to impact. In a recent work we have proposed a high-order Eulerian-Lagrangian finite element method for the simulation of electro-mechanical systems [11, 12, 13]. The Eulerian-
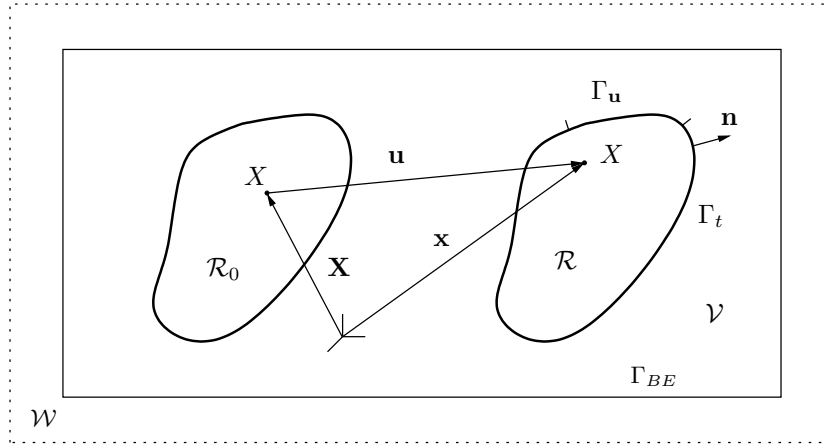
Figure 1: Schematic of the electro-mechanical boundary value problem.

Lagrangian approach has been developed for systems involving highly non-linear deformations and electro-mechanical impact; we employ this earlier work as the framework within which we develop our CSS methodology.

The outline of this paper is as follows. In Section 2, we state the governing equations of the continuum electro-mechanical boundary value problem and our choice of discretization using an Eulerian-Lagrangian finite element method. In Section 3, we discuss the direct algorithmic solution of cyclic steady states in space-time before we test the algorithm for various numerical examples in Section 4.

2 Governing Equations

2.1 Electro-Mechanical Boundary Value Problem

We assume we want to solve the electro-mechanical boundary value problem sketched in Fig. 1. We divide the space into domains $\mathcal{R}$, $\mathcal{V}$ and $\mathcal{W}$: $\mathcal{R}$ should be thought of as a body with boundary Γ, and $\mathcal{V}, \mathcal{W}$ as air or vacuum; note $\mathcal{W}$ represents the far-field domain. In the following, we assume that any magnetic effects are neglected and we assume that the electrical field is quasi-static with respect to the mechanical deformation. In order to solve for the electrical field $\boldsymbol{e}$ in the quasi-static case with a linear dielectric material, we employ an electrical potential Φ, such that $\boldsymbol{e} = -\nabla\Phi$. This leads to the

need to solve Poisson's equation in all space $\mathcal{R}$, $\mathcal{V}$ and $\mathcal{W}$, where we assume the corresponding linear isotropic permittivities $\epsilon_{\mathcal{R}}$, $\epsilon_{\mathcal{V}}$ and $\epsilon_{\mathcal{W}}$. In such a case, and in the absence of any volume charge, one requires

$$\nabla^2 \Phi = 0 \tag{1}$$

in all space, with given Dirichlet boundary data $\Phi = \bar{\Phi}$ along Γ. Here, we limit ourselves to the purely Dirichlet boundary value problem along Γ. Please refer to [11] for a more general discussion of (1) and alternate boundary conditions. The variational form for (1) reads: Find $\Phi \in \mathcal{P}_s$, such that

$$\int_{\mathcal{R}} \epsilon_{\mathcal{R}} \nabla \delta \Phi \cdot \nabla \Phi \mathrm{dv} + \int_{\mathcal{V}} \epsilon_{\mathcal{V}} \nabla \delta \Phi \cdot \nabla \Phi \mathrm{dv} = - \int_{\Gamma_{BE}} \delta \Phi q_{\mathcal{V}} \, \mathrm{da} \tag{2}$$

for all $\delta \Phi \in \mathcal{P}_v$ along with the requirement $\Phi = \bar{\Phi}$ on Γ. We note the coupling to the mechanical displacement $\boldsymbol{u}$ of the body $\mathcal{R}$, which affects the domains $\mathcal{R}$, $\mathcal{V}$, and the boundary Γ. The spaces $\mathcal{P}_s$ and $\mathcal{P}_v$ are suitable subspaces of H^1. The effect of $\mathcal{W}$ is modelled as a far field boundary condition along Γ_{BE} via the boundary element method as described in [11].

For the mechanical problem, we consider a continuum body $\mathcal{R}$ with mass density ρ (see Fig. 1). In the following we will describe the deformation of this body with respect to a reference configuration $\mathcal{R}_0$ at time $t = t_0$. For each material point X in the reference configuration $\mathcal{R}_0$ we associate a vector $\boldsymbol{X} \in \mathbb{R}^3$. For the same material point in $\mathcal{R}$ we associate $\boldsymbol{x} \in \mathbb{R}^3$. Then we define the displacement $\boldsymbol{u}(\boldsymbol{X}, t) \in \mathbb{R}^3$ via the relation $\boldsymbol{x}(\boldsymbol{X}, t) = \boldsymbol{X} + \boldsymbol{u}(\boldsymbol{X}, t)$ for all $t > t_0$. The deformation gradient is given by $\boldsymbol{F} = \partial \boldsymbol{x} / \partial \boldsymbol{X}$, the Jacobian determinant by $J = \det(\boldsymbol{F})$, the right Cauchy-Green tensor by $\mathbf{C} = \mathbf{F}^T \mathbf{F}$, and the left Cauchy-Green tensor by $\boldsymbol{B} = \boldsymbol{F} \boldsymbol{F}^T$. Euler's first law in the coupled theory is given by

$$\rho \ddot{\mathbf{u}} = \mathrm{div} \mathbf{T} + \rho \bar{\mathbf{b}} \qquad \text{in } \mathcal{R} \,, \tag{3}$$

$$\mathbf{u} = \bar{\mathbf{u}} \qquad \text{on } \Gamma_u \,, \tag{4}$$

where $\Gamma_u \subset \Gamma$ is the Dirichlet-boundary for the mechanical problem, $\bar{\mathbf{b}}$ is the body force term, and $\mathbf{T}$ is the total Cauchy stress which satisfies

$$[\![\mathbf{T}]\!] \mathbf{n} = 0 \,, \tag{5}$$

where $[\![\mathbf{T}]\!]$ denotes the jump in the total Cauchy stress across the boundary Γ with normal vector $\boldsymbol{n}$. In this work we assume a linear material polarization, and total Cauchy stress

$$\mathbf{T} = \mathbf{T}_m + \mathbf{T}_e \,, \tag{6}$$

with purely mechanical part

$$\mathbf{T}_m = \rho_0 J^{-1}(\Lambda \ln J - \mu)\boldsymbol{I} + \rho_0 \mu J^{-1}\boldsymbol{B}\,, \tag{7}$$

and electrical part

$$\begin{aligned}
\mathbf{T}_e =& 2\rho_0 c\, J^{-2}\left[1/2(I_1 I_4 - I_2 I_6 - I_5)\boldsymbol{I} + (I_1 I_6 - I_4)\boldsymbol{B} - I_6 \boldsymbol{B}^2\right.\\
& \left. - I_1 \boldsymbol{B}\boldsymbol{e} \otimes \boldsymbol{B}\boldsymbol{e} + \boldsymbol{B}(\boldsymbol{B}\boldsymbol{e} \otimes \boldsymbol{B}\boldsymbol{e}) + (\boldsymbol{B}\boldsymbol{e} \otimes \boldsymbol{B}\boldsymbol{e})\boldsymbol{B}\right] + \mathbf{T}_M\,,
\end{aligned} \tag{8}$$

as detailed in [13]. Furthermore, we denote the small strain Lamé parameters $\Lambda = E\nu/[(1+\nu)(1-2\nu)]$, $\mu = E/[2(1+\nu)]$, the Young's modulus E, the Poisson ratio ν, $c = -(\epsilon_{\mathcal{R}} - \epsilon_0)/(2\rho_0)$, the free-space permittivity ϵ_0, and the identity tensor $\boldsymbol{I}$. The six invariants I_i, $i = 1, \ldots, 6$ are given by

$$I_1 = \mathrm{tr}\mathbf{C}, \ I_2 = \mathrm{tr}\mathbf{C}^*, \ I_3 = \det\mathbf{C}, \tag{9}$$

$$I_4 = \mathrm{tr}\left(\mathbf{C}\mathbf{E} \otimes \mathbf{E}\right), \ I_5 = \mathrm{tr}\left(\mathbf{C}^2 \mathbf{E} \otimes \mathbf{E}\right), \ I_6 = \mathrm{tr}\left(\mathbf{E} \otimes \mathbf{E}\right), \tag{10}$$

with $\mathbf{C}^* = (\det\mathbf{C})\,\mathbf{C}^{-1}$, $\boldsymbol{E} = \boldsymbol{F}^T \boldsymbol{e}$, and the Maxwell stress $\mathbf{T}_M = \epsilon_0\left[\boldsymbol{e} \otimes \boldsymbol{e} - \frac{1}{2}\left(\boldsymbol{e} \cdot \boldsymbol{e}\right)\mathbf{I}\right]$. The mechanical boundary traction due to the external electrical field is given by

$$\mathbf{T}_M^+ \boldsymbol{n} = \epsilon_0 \left[\left(\boldsymbol{e} \cdot \boldsymbol{n}\right)\boldsymbol{e} - \frac{1}{2}||\boldsymbol{e}||^2 \boldsymbol{n}\right] \tag{11}$$

along the Neumann boundary $\Gamma_t \subset \Gamma$, where the superscript $(.)^+$ indicates the limit as we approach the boundary Γ from outside $\mathcal{R}$. From (3) we derive the mechanical weak form: Given initial conditions $\boldsymbol{u}(t_0) = \boldsymbol{u}_0$, $\dot{\boldsymbol{u}}(t_0) = \dot{\boldsymbol{u}}_0$ at $t = t_0$, find $\mathbf{u} \in \mathcal{U}_s$, such that

$$\int_{\mathcal{R}} \delta\mathbf{u} \cdot \rho\ddot{\mathbf{u}}\,\mathrm{dv} + \int_{\mathcal{R}} \nabla\delta\mathbf{u} \cdot \mathbf{T}\,\mathrm{dv} = \int_{\mathcal{R}} \delta\mathbf{u} \cdot \rho\bar{\mathbf{b}}\,\mathrm{dv} + \int_{\Gamma_t} \delta\mathbf{u} \cdot \left(\bar{\mathbf{t}}_a + \mathbf{T}_M^+ \mathbf{n}\right)\mathrm{da}\,, \tag{12}$$

for all admissible variations $\delta\mathbf{u} \in \mathcal{U}_v$ at any $t > t_0$, together with given data $\mathbf{u} = \bar{\mathbf{u}}$ on the Dirichlet boundary Γ_u. Here, $\bar{\mathbf{t}}_a$ is the applied (mechanical) traction due to external forces, and the spaces $\mathcal{U}_s$ and $\mathcal{U}_v$ are suitable subspaces of H^1.

2.2 Semi-Discrete Form

In order to solve (2) and (12) in the context of finite elements, we use a Galerkin discretization for the electrical as well as for the mechanical field.
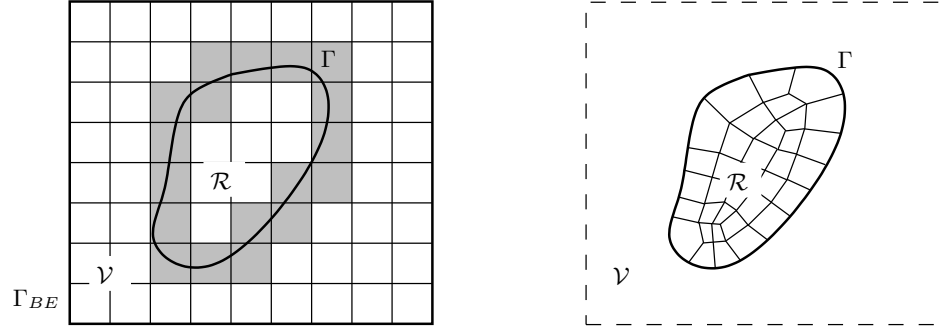
Figure 2: Discretization in space: (left) Eulerian finite element mesh with immersed boundary for the electrical field; (right) Lagrangian finite element mesh for the mechanical motion.

We solve for the mechanical deformation on a Lagrangian grid [Fig. 2(right)], whereas we solve for the electrical field on a fixed Eulerian grid with embedded boundary conditions [Fig. 2(left)]. In order to solve for the electrical potential Φ on a fixed Eulerian grid with embedded boundary conditions, we employ a high-order immersed boundary method as described in [11]. One uses a continuous Galerkin discretization in elements that are not intersected by the boundary Γ. For elements that are intersected by Γ, special elements are employed with an interpolation that follows the boundary shape locally. The discrete form of the electrical quasi-static problem can be stated as: Find $\Phi_{\mathcal{R}}^h, \Phi_{\mathcal{V}}^h \in \mathcal{P}_s^h$, such that

$$\int_{\mathcal{R}} \epsilon_{\mathcal{R}} \nabla \delta\Phi_{\mathcal{R}}^h \cdot \nabla\Phi_{\mathcal{R}}^h \mathrm{dv} + \int_{\mathcal{V}} \epsilon_{\mathcal{V}} \nabla \delta\Phi_{\mathcal{V}}^h \cdot \nabla\Phi_{\mathcal{V}}^h \mathrm{dv} = -\int_{\Gamma_{BE}} \delta\Phi_{\mathcal{V}}^h q_{\mathcal{V}} \mathrm{da} \qquad (13)$$

for all $\delta\Phi_{\mathcal{R}}^h, \delta\Phi_{\mathcal{V}}^h \in \mathcal{P}_v^h$ along with the requirement $\Phi_{\mathcal{V}}^h = \Phi_{\mathcal{R}}^h = \bar{\Phi}$ on Γ^h. Depending on the choice of interpolation in the intersected elements, the requirement $\Phi_{\mathcal{V}}^h = \Phi_{\mathcal{R}}^h = \bar{\Phi}$ on Γ^h is either enforced in a weak sense (e.g. the eXtended finite element method [14, 15]), or in a strong sense (e.g. the immersed boundary discontinuous-Galerkin method, IB-DG [16]). In this work we assume the use of the IB-DG method and that after such efforts, the electrical boundary value problem can be stated as: Find $\mathbf{\Phi}$, such that

$$\boldsymbol{K}(\boldsymbol{U})\mathbf{\Phi} = \boldsymbol{Q}(\boldsymbol{U}), \qquad (14)$$

where the electro-static stiffness $\boldsymbol{K}$, the electrical solution vector $\mathbf{\Phi}$, and the equivalent flux vector $\boldsymbol{Q}$ are assembled in accordance with (13). Note that the

electrical stiffness $\boldsymbol{K}$, as well as the flux vector $\boldsymbol{Q}$ depend on the mechanical deformation vector $\boldsymbol{U}$ due to the change in position of the boundary Γ.

Concerning the solution of the mechanical deformation, we employ a Lagrangian discretization in space [see Fig. 2(right)], and derive the semi-discrete variational form: Find $\mathbf{u}^h \in \mathcal{U}_s^h$, such that

$$\int_{\mathcal{R}} \delta\mathbf{u}^h \cdot \rho\ddot{\mathbf{u}}^h \, \mathrm{dv} + \int_{\mathcal{R}} \nabla\delta\mathbf{u}^h \cdot \mathbf{T}^h \, \mathrm{dv} = \int_{\mathcal{R}} \delta\mathbf{u}^h \cdot \rho\bar{\mathbf{b}} \, \mathrm{dv} + \int_{\Gamma_t} \delta\mathbf{u}^h \cdot \left(\bar{\mathbf{t}}_a + \mathbf{T}_M^+\mathbf{n}\right) \mathrm{da} \,,$$

(15)

for all admissible variations $\delta\mathbf{u}^h \in \mathcal{U}_v^h$ at any $t > t_0$. Let us denote $\boldsymbol{u}^h = \sum_i N_i \boldsymbol{u}_i$, $\dot{\boldsymbol{u}}^h = \sum_i N_i \dot{\boldsymbol{u}}_i$, $\ddot{\boldsymbol{u}}^h = \sum_i N_i \ddot{\boldsymbol{u}}_i$ with $N_i \in \mathcal{U}^h$ and the expansion coefficients $\boldsymbol{U} = [\boldsymbol{u}_i]$, $\dot{\boldsymbol{U}} = [\dot{\boldsymbol{u}}_i]$, $\ddot{\boldsymbol{U}} = [\ddot{\boldsymbol{u}}_i]$. Using a Galerkin discretization, we can bring (15) into the algebraic form: Given $\boldsymbol{U}_0$, $\dot{\boldsymbol{U}}_0$, find $\boldsymbol{U}$ such that

$$\boldsymbol{M}\ddot{\boldsymbol{U}} + \boldsymbol{R}_{div} = \boldsymbol{F}_{ext} \,,$$

(16)

for all time instants $t > t_0$, where $\boldsymbol{M}$ is the mass matrix, $\boldsymbol{R}_{div}$ the stress-divergence term of the mechanical linear momentum balance, and $\boldsymbol{F}_{ext}$ the traction due to external forces. We encounter two types of electrical forces on the continuum: A body force due to internal fields and a surface traction due to the external electrical field. As mentioned earlier, the total Cauchy-stress $\mathbf{T}$ can be split into a purely mechanical part $\mathbf{T}_m$, as well as an electrical part $\mathbf{T}_e$ given by (7) and (8) respectively. Consequently we apply an additive split to $\boldsymbol{R}_{div} = \boldsymbol{R}_{div,m} + \boldsymbol{R}_{div,e}$, where

$$\boldsymbol{R}_{div,m} \leftarrow \int_{\mathcal{R}} \nabla\delta\mathbf{u}^h \cdot \mathbf{T}_m \, \mathrm{dv} \,,$$

(17)

$$\boldsymbol{R}_{div,e} \leftarrow \int_{\mathcal{R}} \nabla\delta\mathbf{u}^h \cdot \mathbf{T}_e \, \mathrm{dv} \,,$$

(18)

with $\boldsymbol{R}_{div,m}$ the classical, purely mechanical stress-divergence term, and $\boldsymbol{R}_{div,e}$ the contribution of electrical body forces. In the following we assume that $\boldsymbol{F}_{ext}$ is split into

$$\boldsymbol{F}_{ext} = \boldsymbol{F}_{contact} + \boldsymbol{F}_{dis} + \boldsymbol{F}_M^+ \,,$$

(19)

viz., the surface traction $\boldsymbol{F}_{contact}$ due to mechanical contact, the dissipative force $\boldsymbol{F}_{dis}$ for example due to friction or absorbing boundary conditions, and the surface traction $\boldsymbol{F}_M^+$ due to external electrical fields. We are omitting any other applied forces that have been introduced via $\bar{\boldsymbol{t}}_a$ for the sake of simplicity.

2.3   Algorithmic Solution of the Coupled System

For future reference, let us define

$$\boldsymbol{R}(\boldsymbol{U}, \boldsymbol{\Phi}) = \boldsymbol{R}_{div,m}(\boldsymbol{U}) + \boldsymbol{R}_{div,e}(\boldsymbol{U}, \boldsymbol{\Phi}) - \boldsymbol{F}_M^+(\boldsymbol{U}, \boldsymbol{\Phi}) - \boldsymbol{F}_{contact}(\boldsymbol{U}) \,. \quad (20)$$

We account for any dissipative effects by an explicit linear model with a damping matrix $\boldsymbol{D}$, such that we can bring (16), (14) in the form: Given $\boldsymbol{U}_0$, $\dot{\boldsymbol{U}}_0$, find $(\boldsymbol{U}, \boldsymbol{\Phi})$ such that

$$\boldsymbol{M}\ddot{\boldsymbol{U}} + \boldsymbol{D}\dot{\boldsymbol{U}} + \boldsymbol{R}(\boldsymbol{U}, \boldsymbol{\Phi}) = \boldsymbol{0} \,, \quad (21)$$

$$\boldsymbol{K}(\boldsymbol{U})\boldsymbol{\Phi} = \boldsymbol{Q}(\boldsymbol{U}) \,, \quad (22)$$

for all time instants $t > t_0$. This states the coupled nonlinear semi-discrete system. In order to integrate equations (21) and (22) in time, we will examine both an implicit method (mid-point rule) as well as an explicit method (centered-difference scheme), for which the algorithmic enforcement of dynamical contact is discussed in [12, 13].

For the dynamical implicit solution we employ the *mid-point rule*. Let $\boldsymbol{U}_n \equiv \boldsymbol{U}(t_n)$, $\dot{\boldsymbol{U}}_n \equiv \dot{\boldsymbol{U}}(t_n)$, $\ddot{\boldsymbol{U}}_n \equiv \ddot{\boldsymbol{U}}(t_n)$, $\boldsymbol{\Phi}_n \equiv \boldsymbol{\Phi}(t_n)$ at $t = t_n$. Then for one step $(t_n, t_{n+1}]$ we require: Given $\boldsymbol{U}_n$, $\dot{\boldsymbol{U}}_n$, and Δt_n, find $\boldsymbol{U}_{n+1}$, $\dot{\boldsymbol{U}}_{n+1}$ such that

$$\boldsymbol{M}\ddot{\boldsymbol{U}}_{n+1/2} + \boldsymbol{D}\dot{\boldsymbol{U}}_{n+1/2} + \boldsymbol{R}(\boldsymbol{U}_{n+1/2}, \boldsymbol{\Phi}_{n+1/2}) = \boldsymbol{0} \,, \quad (23)$$

$$\boldsymbol{K}(\boldsymbol{U}_{n+1/2})\boldsymbol{\Phi}_{n+1/2} = \boldsymbol{Q}(\boldsymbol{U}_{n+1/2}) \,, \quad (24)$$

where

$$\boldsymbol{\Phi}_{n+1/2} = (\boldsymbol{\Phi}_{n+1} + \boldsymbol{\Phi}_n)/2 \,, \quad (25)$$

$$\boldsymbol{U}_{n+1/2} = (\boldsymbol{U}_{n+1} + \boldsymbol{U}_n)/2 \,, \quad (26)$$

$$\dot{\boldsymbol{U}}_{n+1/2} = (\boldsymbol{U}_{n+1} - \boldsymbol{U}_n)/\Delta t_n \,, \quad (27)$$

$$\ddot{\boldsymbol{U}}_{n+1/2} = (2/\Delta t_n^2)(\boldsymbol{U}_{n+1} - \boldsymbol{U}_n) - (2/\Delta t_n)\dot{\boldsymbol{U}}_n \,. \quad (28)$$

This method is second-order accurate and unconditionally stable for linear systems. At each time-step one has to solve the fully coupled nonlinear problem by an iterative method. To this end, we use a staggered scheme, and a mass lumping procedure following [17, p.704] together with a Newton iterator. In this setting, for each time-step and each iteration of the Newton-Raphson method, one first calculates the electrical field for a fixed mechanical

configuration, and subsequently the resulting electrical forces are updated in this configuration in order to drive the mechanical displacement.

For the dynamical explicit solution we investigate the *centered-difference scheme* (e.g. [18, p.490]): Given $\boldsymbol{U}_n$, $\dot{\boldsymbol{U}}_n$, $\ddot{\boldsymbol{U}}_n$ and Δt_n, for one step $(t_n, t_{n+1}]$ we require:

$$\boldsymbol{M}\ddot{\boldsymbol{U}}_{n+1} + \boldsymbol{D}\dot{\boldsymbol{U}}_{n+1} + \boldsymbol{R}(\boldsymbol{U}_{n+1}, \boldsymbol{\Phi}_{n+1}) = \boldsymbol{0}\,, \tag{29}$$

$$\boldsymbol{K}(\boldsymbol{U}_{n+1})\boldsymbol{\Phi}_{n+1} = \boldsymbol{Q}(\boldsymbol{U}_{n+1})\,, \tag{30}$$

and

$$\boldsymbol{U}_{n+1} = \boldsymbol{U}_n + \Delta t_n \dot{\boldsymbol{U}}_n + (\Delta t_n^2/2)\ddot{\boldsymbol{U}}_n\,, \tag{31}$$

$$\dot{\boldsymbol{U}}_{n+1} = \dot{\boldsymbol{U}}_n + (\Delta t_n/2)\left[\ddot{\boldsymbol{U}}_n + \ddot{\boldsymbol{U}}_{n+1}\right]\,. \tag{32}$$

This scheme is second-order accurate and conditionally stable. One requires a sufficiently small time-step, such that the Courant condition is satisfied. Following [19], one typically chooses

$$\Delta t_n = \delta_c \frac{h}{v_p}\,, \tag{33}$$

with the element size h of the smallest element, and the p-wave speed v_p which can be estimated for a linear elastic material by $v_p = \sqrt{2\mu/\rho + \Lambda/\rho}$, where Λ and μ are the first and second Lamé-parameters. In the following we assume the empirical factor $\delta_c = 0.9$. Since the scheme is explicit, we can solve the electrical and mechanical problem independently and only encounter linear equations. Thus the explicit method is computationally more efficient in comparison to the implicit method when the time-steps are comparable. Note however, that the stability requirement (33) must be satisfied, which imposes a restriction on the method and may require much smaller time-steps as compared to the implicit method.

When exciting the system (21), (22) by a periodic load, one may encounter a cyclic steady state if the damping is sufficient. In order to find steady state solutions to (21), (22), one traditionally evolves (21), (22) from initial conditions $\boldsymbol{U}_0$, $\dot{\boldsymbol{U}}_0$, typically zero conditions, until a steady state is reached. We term this methodology the naïve time-stepping method, alternately the full time-stepping (FTS) method. Such time-stepping through the transient phase will be very expensive for systems with low damping. In the following we investigate a method, that enables one to find steady state solutions directly – without the need to fully step through the entire transient phase.

3   Cyclic Steady State Solutions

Our focus in this study is on systems that are excited by an electrical field in resonance with one of the system's vibrational modes. For linear problems, such problems are easily approached via traditional modal analysis; see e.g. [17, p.580]. However, in the nonlinear setting one requires alternative methodologies. Here we will propose a direct numerical solution, in order to find steady state solutions of the fully coupled nonlinear problem excited at a given resonance frequency without the need to resort to the FTS method.

3.1   Direct Solution of Cyclic Steady States

The steady state solution of interest arises from equations (21), (22) when they are subjected to harmonic excitation. In the following we assume that the damping is sufficient such that the system will reach a cyclic steady state for a harmonic load, typically as part of the potential boundary conditions. In order to find cyclic steady state solutions for the nonlinear coupled system excited at frequency ω, we consider the method advocated in [5, 6]. In our case the period is given by $T = 2\pi/\omega$, where the mechanical state is represented by $\boldsymbol{X} = [\boldsymbol{U}; \dot{\boldsymbol{U}}]$. The CSS problem reads: Given a period T, find $\boldsymbol{X}_0$ such that

$$\boldsymbol{H}(\boldsymbol{X}_0) = \boldsymbol{X}(T) - \boldsymbol{X}_0 = \boldsymbol{0} \,, \tag{34}$$

where $\boldsymbol{X}(T)$ evolves according to (21), (22) with initial conditions $\boldsymbol{X}_0$.[1] Put simply, the CSS problem amounts to finding the initial conditions such that the nonlinear system evolves back to them within one period. The solution to (34) will be found using the Newton-Raphson method: Given a guess $\boldsymbol{X}_0^i$, we update $\boldsymbol{X}_0^{i+1} = \boldsymbol{X}_0^i + \Delta\boldsymbol{X}_0^i$, where we find $\Delta\boldsymbol{X}_0^i$, such that

$$D\boldsymbol{H}[\boldsymbol{X}_0^i](\Delta\boldsymbol{X}_0^i) = -\boldsymbol{H}(\boldsymbol{X}_0^i) \,. \tag{35}$$

Here the application of the tangent operator means

$$D\boldsymbol{H}[\boldsymbol{X}_0](\Delta\boldsymbol{X}_0) = \Delta\boldsymbol{X}(T) - \Delta\boldsymbol{X}_0 \,, \tag{36}$$

where $\Delta\boldsymbol{X}(T)$ is found by evolving the linearized equation

$$\boldsymbol{M}\Delta\ddot{\boldsymbol{U}} + \boldsymbol{D}\Delta\dot{\boldsymbol{U}} + \frac{\partial\boldsymbol{R}}{\partial\boldsymbol{U}}(\boldsymbol{U}, \boldsymbol{\Phi})\Delta\boldsymbol{U} = \boldsymbol{0} \,, \tag{37}$$

---

[1] Note that one could also treat the period T as an additional unknown to solve for, but here we assume T as a given parameter matching the excitation frequency of the external load.

over one period starting from initial conditions $\Delta \boldsymbol{X}_0$ along the path $\boldsymbol{X}(t)$ that is determined from (21), (22) with initial conditions $\boldsymbol{X}_0$.

In order to assemble the operator $D\boldsymbol{H}[\boldsymbol{X}_0]$ in each Newton step, one may iteratively calculate each column $D\boldsymbol{H}[\boldsymbol{X}_0]_{:,i}$ via

$$D\boldsymbol{H}[\boldsymbol{X}_0]_{:,i} = D\boldsymbol{H}[\boldsymbol{X}_0](\boldsymbol{e}_i), \tag{38}$$

with basis vectors $\boldsymbol{e}_i \in \mathbb{R}^N$ ($i = 1, \ldots, N$), where N is the length of $\boldsymbol{X}$. While this gives the full operator for a direct solution of (35), the assembly via (38) is expensive. As advocated in [6], we instead employ the generalized minimal residual method (GMRES) so that only the application of the operator is needed. To this end let us denote $A = D\boldsymbol{H}[\boldsymbol{X}_0^i]$, $b = -\boldsymbol{H}(\boldsymbol{X}_0^i)$ and $x = \Delta \boldsymbol{X}_0^i$, so that for each Newton step 'i' we wish to solve $Ax = b$. In the proposed scheme, one computes the m-th order Krylov subspace $\mathcal{K}_m = \text{span}\{b, Ab, A^2 b, \ldots, A^{m-1} b\}$ by a standard Arnoldi iteration. The minimizer of the residual $||Ax - b||_2$ over $\mathcal{K}_m$ gives the approximate solution which we set to $\Delta \boldsymbol{X}_0^i$. For each Newton step, one has to compute (34) by evolving (21), (22) with initial conditions $\boldsymbol{X}_0^i$. Subsequently, one evolves (37) ($m - 1$) times with multiple initial conditions $b, Ab, \ldots, A^{m-2} b$ in order to construct the Krylov subspace within which an approximate solution to (35) is found. In this work we find the dimension m, by requiring $||Ax - b||/||b|| < 10^{-3}$ during the Arnoldi iteration as in [6]. The algorithm is summarized in Alg. 1. We refer to [20] for a more detailed discussion on GMRES and Arnoldi iterations.

4   Numerical Examples

In the following examples we will consider that a cyclic steady state is reached, when the relative L2-norm of $\boldsymbol{H}(t_n) = \boldsymbol{X}(t_n) - \boldsymbol{X}(t_n - T)$ after a period T,

$$\text{Residual} = \sqrt{\frac{\sum_i |X_i(t_n) - X_i(t_n - T)|^2}{\sum_i |X_i(t_n)|^2}}, \tag{39}$$

is converged by six orders of magnitude. All accuracy considerations have been done within this scope. Note that another tolerance setting will change the accuracy requirements on the discretization, and results will differ from the current study.

Cyclic Steady State Solution

Given $\boldsymbol{X}_0^0 = [\boldsymbol{U}_0^0, \dot{\boldsymbol{U}}_0^0]$.
LOOP i
1. Calculate $\boldsymbol{H}(\boldsymbol{X}_0^i)$ according to (34), (21) and (22).
2. Iteratively form m-th order Krylov subspace by an Arnoldi iteration and computing $D\boldsymbol{H}[\boldsymbol{X}_0^i](.)$ according to (36) and (37).
3. Find the minimizer $\tilde{\boldsymbol{X}}$ of the residual $||D\boldsymbol{H}[\boldsymbol{X}_0^i](\tilde{\boldsymbol{X}}) + \boldsymbol{H}(\boldsymbol{X}_0^i)||_2$ over $\mathcal{K}_m$ by a least-square approximation.
4. Set $\Delta\boldsymbol{X}_0^i = \tilde{\boldsymbol{X}}$.
5. Check convergence $||\Delta\boldsymbol{X}_0^i||_2/||\boldsymbol{X}_0^i||_2 < TOL$ and update if needed
   $\boldsymbol{X}_0^{i+1} = \boldsymbol{X}_0^i + \Delta\boldsymbol{X}_0^i$.

Algorithm 1: Cyclic steady state solution via GMRES.

4.1   Critical Time-step

In order to obtain accurate results and optimal convergence rates, it is crucial to ensure a converged discretization in the time-domain. In our examples we require the finite element solution at steady state to be converged by six orders of magnitude. Given a linearized damping ratio ξ, we find the number of time-steps per cycle $T/\Delta t_n$ for the centered-difference scheme and for the mid-point rule by monitoring the residual (39), such that convergence is achieved. In addition, the requirement (33) must be met when using the explicit time-stepper.

4.2   Nanotube Vibration

Our first example deals with a carbon nanotube that is excited by an external electrical field. As discussed in [13], carbon nanotubes possess very unique and promising characteristics for use as NEMS resonators [21, 22, 2, 23, 24]. In this study we suppose that the carbon nanotube is a conductor. After certain corrections when extracting material properties, the use of continuum mechanics is still justified for such systems [25], and various mechanical models exist [26, 27]. We focus here on the efficient simulation of the first three cyclic modes of vibration of a nanotube as sketched in Fig. 3 via Alg. 1. In this study we consider a nanotube with a sharp corner. While carbon

nanotubes may be closed smoothly at the tip, the cut-nanotube imposes a greater challenge on the computational treatment due the singularity that arises in the electrical field at the corner. We demonstrate the necessity of a high-order IB-DG in such a case, in order to achieve convergence of Alg. 1.

4.2.1 Fully transient solution method: Nanotube

For analysis purposes we will consider a very coarse discretization such that we can also consider the fully transient solution (FTS) method. As sketched in Fig. 3, we assume that the nanotube is mechanically clamped and electrically grounded. A separate input voltage V_i at an external electrode creates a capacitive force across the gap, such that the nanotube will vibrate. The input voltage is given by

$$V_i(t) = V_{\mathrm{DC}} + V_{\mathrm{AC}} \sin \omega_i t \,, \tag{40}$$

with constant part V_{DC}, alternating amplitude V_{AC}, and frequencies ω_i, $i = 1, 2, 3$. The ω_i represent the linearized eigen-frequencies about the static deformation resulting from V_{DC}. For the numerical example we consider a nanotube length of 80 nm and a diameter of 8 nm. The initial gap to the electrode is 46 nm, and we assume a nonlinear Neo-Hookean material as in (7) with $E = 1$ TPa, $\nu = 0.31$, $\rho = 1$ g/cm^3. The resulting linearized eigen-frequencies are summarized in Tab. 1 in accordance with an ultra-high frequency resonator [28]. We assume a mass-proportional damping $\boldsymbol{D} = \alpha_M \boldsymbol{M}$, with $\alpha_M \in \{5 \cdot 10^9 \text{ s}^{-1}, 10 \cdot 10^9 \text{ s}^{-1}\}$. Then, the linearized damping ratios are given by $\xi_i = \alpha_M/(2\omega_i)$ as tabulated in Tab. 1 for linearized Mode 1-3 excitations. Note in this study we limit ourselves to a 20×2 finite element grid for the mechanical motion in order to calculate the fully transient response, which already sets a limit of > 1443 time-steps per cycle according to (33) for the fundamental mode in the explicit case. One would need to consider a mesh refinement, and/or the use of enhanced elements or incompatible modes in order to gain more accurate results in such a bending dominated problem. Such methods are well established, and we refer to [29] for a brief historical account and references therein. For the electrical field we use a 25×25 Eulerian finite element grid, in combination with the high-order IB-DG method to accurately evaluate the singularity of the boundary traction around the nanotube corner. In Tab. 1(bottom, $\alpha_M = 10 \cdot 10^9$ s^{-1}) we monitor the number of time-steps per cycle $T_i/\Delta t_n = 2\pi/(\omega_i \Delta t_n)$ for the explicit and implicit method to reach steady state, as well as the total

Mode 1 ($f_1 = 7.2$ GHz)   Mode 2 ($f_2 = 42.6$ GHz)   Mode 3 ($f_3 = 111.2$ GHz)
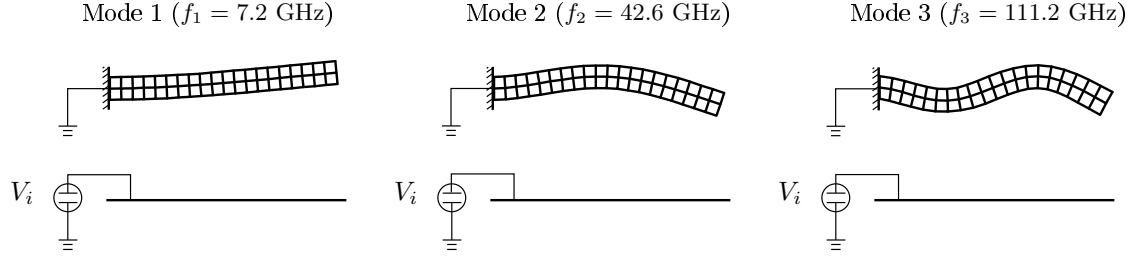

Figure 3: Nanotube vibration schematic showing mode shapes and linearized vibrational frequencies.

computational time T_{CPU} in our MATLAB implementation. The implicit method is seen to be more efficient in this example for the simulation of the lower modes since it is unconditionally stable, and larger time-steps may be used as long as accuracy is preserved. For the higher modes, requirement (33) imposes less restriction on the stability region, and the explicit method will be more efficient in comparison to the mid-point rule as we observed higher accuracy for similar time-step sizes. In the remaining discussion we will limit our discussion to the use of explicit time-stepping for both the CSS and the FTS methods.

Since in our case we employ mass-proportional damping, the damping ξ_i becomes smaller for a fixed α_M at higher excitation frequencies. The direct consequence of this is that, as shown in Tab. 1, the number of cycles to overcome the transient phase to a steady state is relatively higher at higher excitation frequencies. As mentioned earlier, we assume that a steady state is reached when the residual (39) is converged by six orders of magnitude.

Figure 4 shows a typical result for a first mode excitation with $\xi_1 = 5.6 \cdot 10^{-2}$, $V_{\mathrm{DC}} = 60$ V and $V_{\mathrm{AC}} = 40$ V after 40 cycles of oscillation with zero initial conditions. One can observe the deformed mechanical mesh, the electrical potential field, as well as the Maxwell boundary traction at various time instants. Note that such large motions can be easily tracked with the immersed boundary method, and no remeshing or motion of the electrical mesh is required – as becomes necessary when using a Lagrangian or arbitrary Eulerian-Lagrangian (ALE) approach. Note moreover, that the boundary force around the corner stems from a singular charge distribution; this is well captured by our chosen IB-DG method.

In Fig. 5 we monitor the vertical tip displacement and velocity for the case $\alpha_M = 5 \cdot 10^9$ s^{-1} with loading $V_{\mathrm{DC}} = 60$ V and $V_{\mathrm{AC}} = 40$ V. The results

$\alpha_M = 5 \cdot 10^9$ s^{-1}	f_i[GHz]	ξ_i	N_i	$T_i/\Delta t_n^{expl}$	T_{CPU}^{expl}[h]		
Mode 1:	7.2	$5.6 \cdot 10^{-2}$	40	1444	78.8		
Mode 2:	42.6	$9.4 \cdot 10^{-3}$	238	244	81.0		
Mode 3:	111.2	$3.6 \cdot 10^{-3}$	621	96	82.7		
$\alpha_M = 10 \cdot 10^9$ s^{-1}	f_i[GHz]	ξ_i	N_i	$T_i/\Delta t_n^{expl}$	T_{CPU}^{expl}[h]	$T_i/\Delta t_n^{impl}$	T_{CPU}^{impl}[h]
Mode 1:	7.2	$1.1 \cdot 10^{-1}$	20	1444	42.1	36	3.0
Mode 2:	42.6	$1.9 \cdot 10^{-2}$	119	244	42.1	88	43.3
Mode 3:	111.2	$7.2 \cdot 10^{-3}$	310	96	42.6	144	184.8

Table 1: Nanotube vibration example: linearized eigenfrequencies f_i, damping ratios ξ_i, number of cycles N_i to reach steady state during the fully transient solution; (top, $\alpha_M = 5 \cdot 10^9$ s^{-1}) explicit time-step size $T_i/\Delta t_n$ (steps per cycle) and computational time T_{CPU} for linearized Mode $i = 1 - 3$ excitations; (bottom, $\alpha_M = 10 \cdot 10^9$ s^{-1}) additionally a comparison between explicit and implicit time-step size $T_i/\Delta t_n$ and computational time T_{CPU}.
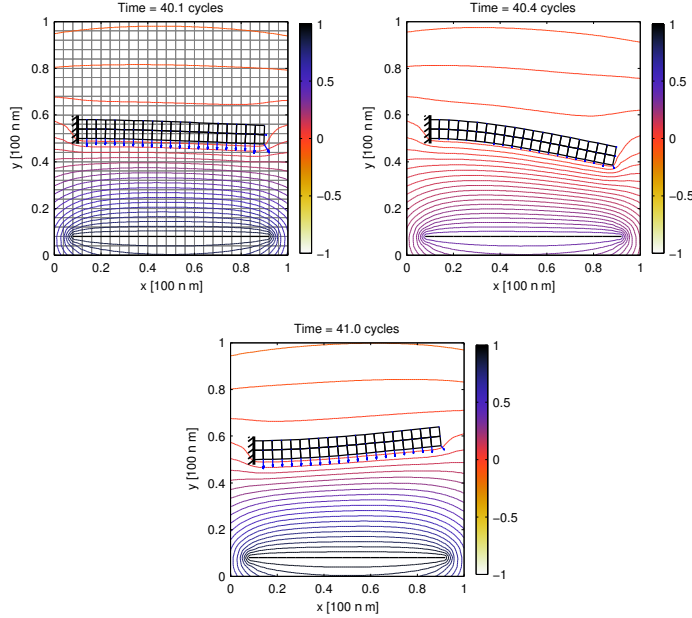
Figure 4: Nanotube vibration, Mode 1 excitation: deformed mechanical (bold) mesh, electrical (fine) mesh, contour of electrical potential, and Maxwell boundary traction at $V_{DC} = 60$ V and $V_{AC} = 40$ V for various time instants.
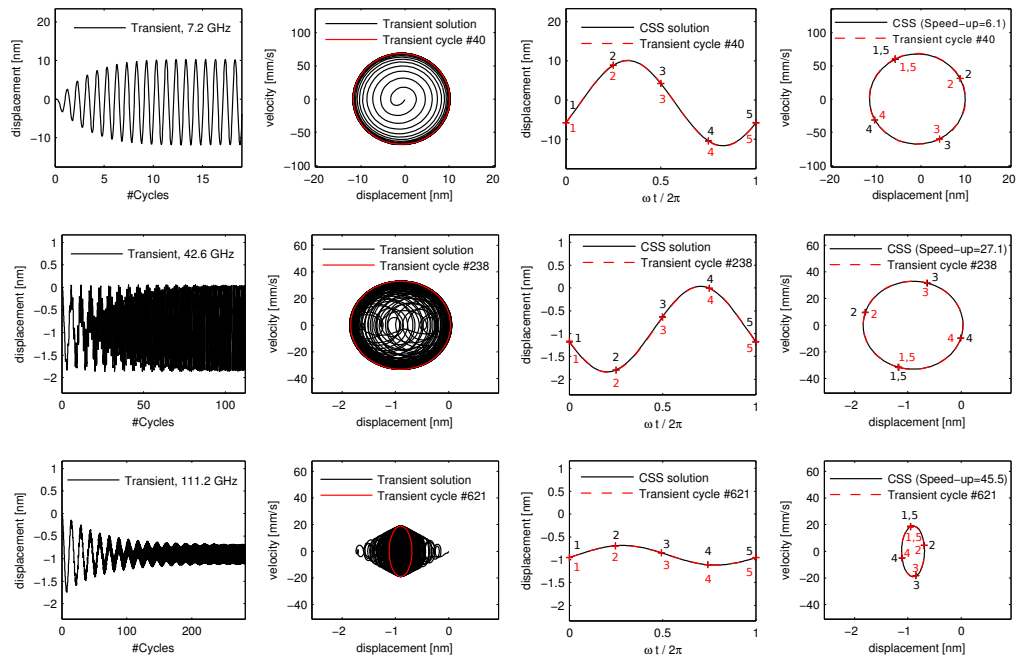
Figure 5: Nanotube vibration: fully transient solution (FTS) and cyclic steady state solution (CSS) via GMRES (Alg. 1) of the tip-displacement and velocity for (top) Mode 1 excitation, (middle) Mode 2 excitation, (bottom) Mode 3 excitation.

over time and the corresponding phase portraits are plotted in columns 1 and 2 for Mode 1-3 excitations when we start from zero initial conditions. The displacement with Mode 1 excitation reaches about -0.9 ± 11 nm and a velocity of ± 68 mm/s at steady state after 40 cycles [Fig. 5(top)]. Looking at the higher mode excitations, the amplitude of the displacement at steady state decreases to about -0.9 ± 0.9 nm for Mode 2 excitation after 238 cycles [Fig. 5(middle)] and -0.9 ± 0.2 nm for Mode 3 excitation after 621 cycles [Fig. 5(bottom)]; the velocity decreases to about ± 33 mm/s for Mode 2 excitation and ± 19 mm/s for Mode 3 excitation. Note that the simulation of the higher modes becomes more expensive, as the number of cycles to overcome the transient phase increases due to the lower damping. For even lower damping or finer meshes, the simulation time to overcome the transient phase will impose severe limitations on the design process if the FTS method is used.

4.2.2 CSS method: Nanotube

We now employ Alg. 1 in order to find solutions to (34) more efficiently. As for the FTS, we have employed the explicit time-integration scheme to evolve (21) as well as (37) with time-step size in accordance to Tab. 1. After finding the initial conditions $\boldsymbol{X}_0$ according to Alg. 1, we have evolved equations (21) and (22) with these initial conditions over one period T in order to compare the results to the FTS method; see Fig. 5, columns 3 and 4. The direct solution via Alg. 1 shows excellent agreement when compared to the full time-stepping through the transient phase from zero initial conditions. In Fig. 5 we have also labeled various corresponding time-instants $1-5$ in the steady state displacement [Fig. 5(third column)] and in the phase portrait [Fig. 5(fourth column)] to assist in comparison.

In Fig. 6(top) we plot the residual from the FTS scheme [Fig. 6(top, left)], as well as from the proposed CSS scheme via Alg. 1 [Fig. 6(top,right)] at various damping values. While the number of cycles to reach convergence in the transient solution increases for lower damping values, the number of Newton iterations of the CSS solution remained at about $5-6$ Newton iterations, largely independent of damping. We show the numerical values of the Newton residual of the CSS solution and the size of the Krylov subspace in Tab. 2 for the case $\alpha_M = 5 \cdot 10^9$ s^{-1} as plotted in Fig. 6(top,right), as well as for the case $\alpha_M = 10 \cdot 10^9$ s^{-1}. In both cases, we typically encounter convergence by six orders of magnitude within 4 to 6 iterations.
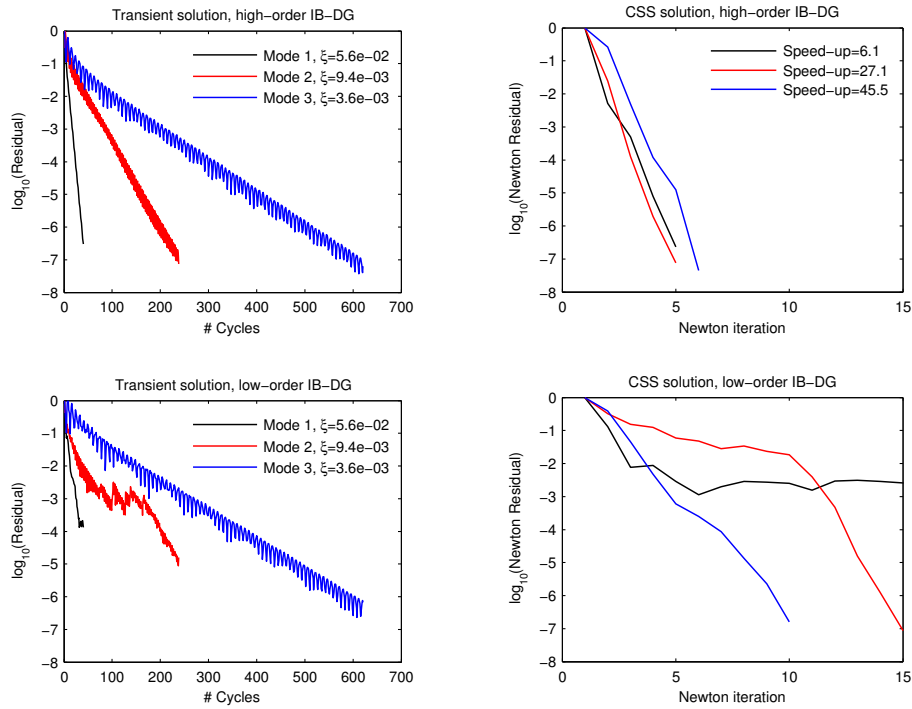
Figure 6: Nanotube vibration: (top) convergence of the residual (39) when using the high-order IB-DG for (left) the fully transient solution (FTS) and (right) the cyclic steady state solution (CSS) via GMRES (Alg. 1); (bottom) convergence issues of the low-order IB-DG.

$\alpha_M = 5 \cdot 10^9$ s^{-1}	Mode 1 $\|\Delta \boldsymbol{X}_0^j\|_2/\|\boldsymbol{X}_0^j\|_2$	m_j	Mode 2 $\|\Delta \boldsymbol{X}_0^j\|_2/\|\boldsymbol{X}_0^j\|_2$	m_j	Mode 3 $\|\Delta \boldsymbol{X}_0^j\|_2/\|\boldsymbol{X}_0^j\|_2$	m_j
$j = 1$	$1.0 \cdot 10^0$	6	$1.0 \cdot 10^0$	24	$1.0 \cdot 10^0$	26
2	$5.1 \cdot 10^{-3}$	16	$2.4 \cdot 10^{-2}$	52	$2.6 \cdot 10^{-1}$	63
3	$5.0 \cdot 10^{-4}$	16	$1.3 \cdot 10^{-4}$	77	$4.9 \cdot 10^{-3}$	111
4	$7.9 \cdot 10^{-6}$	19	$1.9 \cdot 10^{-6}$	81	$1.2 \cdot 10^{-4}$	244
5	$2.3 \cdot 10^{-7}$	14	$7.5 \cdot 10^{-8}$	81	$1.3 \cdot 10^{-5}$	244
6					$4.4 \cdot 10^{-8}$	244

$\alpha_M = 10 \cdot 10^9$ s^{-1}	Mode 1 $\|\Delta \boldsymbol{X}_0^j\|_2/\|\boldsymbol{X}_0^j\|_2$	m_j	Mode 2 $\|\Delta \boldsymbol{X}_0^j\|_2/\|\boldsymbol{X}_0^j\|_2$	m_j	Mode 3 $\|\Delta \boldsymbol{X}_0^j\|_2/\|\boldsymbol{X}_0^j\|_2$	m_j
$j = 1$	$1.0 \cdot 10^0$	5	$1.0 \cdot 10^0$	18	$1.0 \cdot 10^0$	20
2	$3.2 \cdot 10^{-3}$	9	$2.8 \cdot 10^{-2}$	35	$6.2 \cdot 10^{-1}$	54
3	$1.0 \cdot 10^{-4}$	10	$5.4 \cdot 10^{-5}$	45	$7.1 \cdot 10^{-3}$	68
4	$3.1 \cdot 10^{-6}$	10	$3.9 \cdot 10^{-7}$	49	$1.7 \cdot 10^{-4}$	87
5	$5.3 \cdot 10^{-9}$	10			$1.3 \cdot 10^{-6}$	95
6					$9.2 \cdot 10^{-8}$	102

Table 2: Nanotube vibration example: residual convergence $\|\Delta \boldsymbol{X}_0^j\|_2/\|\boldsymbol{X}_0^j\|_2$ of Alg. 1 for Mode 1-3 excitations and number of Arnoldi iterations m_j for each Newton step j and various α_M.

We have measured the speed-up S which we define as the computational time $T_{\text{transient}}$ that is required to evolve equations (21) and (22) from zero initial conditions until the residual (39) is converged by six orders of magnitude divided by the computational time T_{css} that is required to find convergence of (39) by six orders of magnitude via Alg. 1:

$$S = \frac{T_{\text{transient}}}{T_{\text{css}}} \,.$$ (41)

For this example we see speed-ups ranging from $S = 3.3$ for Mode 1 excitation at $\xi_1 = 1.1 \cdot 10^{-1}$ all the way up to $S = 45.5$ for Mode 3 excitation at $\xi_3 = 3.6 \cdot 10^{-3}$. Please see Section 4.4 for a further discussion of these results.

4.2.3   Comparison to Low-order Method

In the example just presented, we used a high-order immersed boundary method. It is instructive to observe what happens if one uses instead a low-order immersed boundary method [16, 11]. Fig. 6(bottom) displays the algorithmic performance with the use of a low-order IB-DG; this is seen to result in reduced or even incomplete convergence of the residual for the FTS method [Fig. 6(bottom,left)], as well as for the CSS solution [Fig. 6(bottom,right)]. Such observations are consistent to what has been previously observed in [11] and indicate to us the necessity of a higher-order accurate immersed boundary method in this example with a singular electric field. The high-order IB-DG is needed not only for accuracy and physically meaningful results, but also for obtaining convergence during the Newton iteration of the cyclic steady state solution via Alg. 1.

4.3   Reso-switch

Our second example examines a micro-electro-mechanical disk resonator, which is excited in the wine-glass mode by a forced vibration such that dynamic contact occurs with a rigid electrode as sketched in Fig. 7. Such on-chip resonators or dynamic switches show high potential for the replacement of transistors, e.g. for power-amplification, due to their superior quality factors (low damping properties) [30, 31, 3, 4]. The system is similar to the resonance switch (reso-switch) in the work by [1].

As sketched in Fig. 7, we assume that the driving electrodes are operated at a periodic input voltage V_i, and the resulting capacitive force brings the
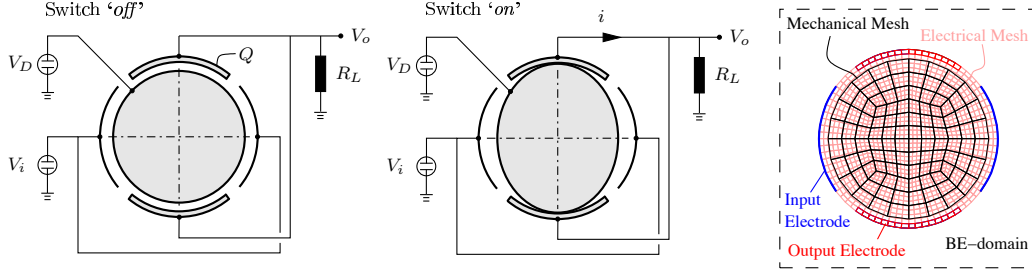
Figure 7: Reso-switch example: (left) schematic '*off*'-mode; (middle) schematic '*on*'-mode; (right) mechanical mesh, electrical mesh, input/output electrodes, and boundary element (BE) domain.

disk into a resonant vibration mode. The voltage at the disk is kept constant at V_D. During this vibration mode, the disk will periodically switch contact with the output electrodes, where a voltage V_o is measured. No contact along the input axis occurs due to a larger air-gap in comparison to the output axis. During '*off*'-mode, an electrical charge Q assembles on the electrodes, whereas a current i flows when the disk touches the electrodes, or during electrical breakdown.

In the context of finite elements, we find the linearized eigenmodes numerically by a standard subspace iteration [32, p.156]. The calculation is done assuming quarter-symmetry, as our mode of interest has quarter-symmetry. For the mechanical deformation of the disk we employ 108 quadrilateral elements with a bi-linear interpolation [see Fig. 7(right)], and a plane stress nonlinear Neo-Hookean material model as derived from (7) with standard material properties of Nickel: $E = 179$ GPa, $\nu = 0.31$, $\rho = 8.9$ g/cm^3. For a disk radius $R = 70$ μm and thickness 4 μm, we obtain the linearized fundamental frequency $f_0 = 14.8$ MHz.

For the electrical field computation, we use a background mesh with 1200 quadrilateral elements that cover the domain of interest as sketched in Fig. 7(right). The electrode boundaries are aligned with the background mesh, and the boundary motion of the disk is captured by the immersed boundary method. We apply a resonant load at the input electrodes:

$$V_i(t) = V_{\mathrm{DC}} + V_{\mathrm{AC}} \sin \omega t \,, \tag{42}$$

where $\omega = 2\pi f_0$, the bias-voltage is given by V_{DC}, and the load amplitude is V_{AC}. At the output electrodes we assume $V_o = V_D$ when the disk is in
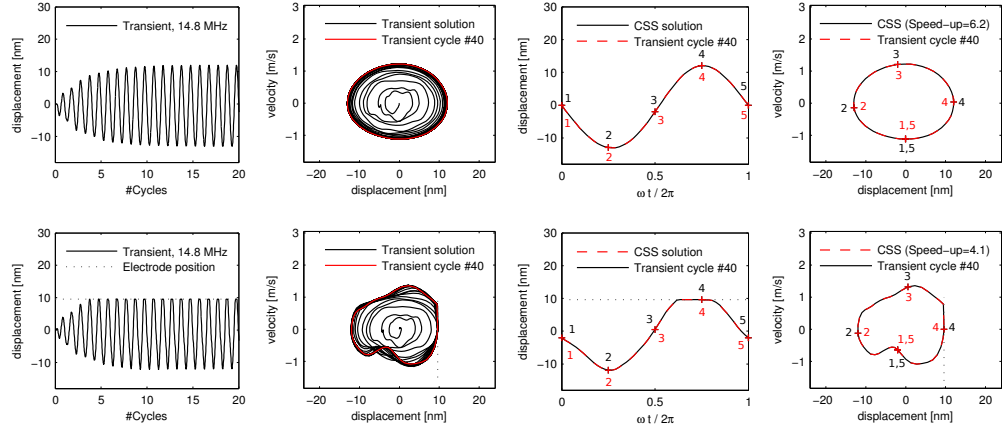
Figure 8: Reso-switch example: transient solution and cyclic steady state solution (CSS) via GMRES (Alg. 1) of the top-disk-node displacement and velocity for (top) *Case 1*, and (bottom) *Case 2*.

contact or during electrical breakdown ('*on*'-mode), and otherwise calculate V_o from the requirement

$$\frac{dQ}{dt} = \frac{V_o}{R_L} \, , \tag{43}$$

where the output load $R_L = 220 \ \Omega$ and the total charge Q on both output electrodes is calculated from the electrical field (see [13]). The damping is assumed to be mass-proportional with $\boldsymbol{D} = \alpha_M \boldsymbol{M}$, such that the linearized damping ratio is $\xi = \alpha_M/(2\omega)$. In the following example we test the case $\xi = 5.6 \cdot 10^{-2}$. Note that the mesh densities are artificially low so that we have easy access to the FTS solution for comparison purposes.

4.3.1   FTS method: Reso-Switch

As with the nanotube example we will begin our discussion of the reso-switch by looking at the transient full time-stepping method from zero initial conditions. We will do so looking at two separate cases, one that leads to contact and one that does not.

Case 1: First we will excite the disk at a load $V_{DC} = 6.45$ kV, $V_{AC} = 4.3$ kV and $V_D = 240$ V with the initial gap to the output electrodes being $g_0 = 2.2 \ \mu$m, and the initial gap between the input electrodes and the disk being 6 μm. With this load there will be no contact with the output

electrodes as the displacement does not sufficiently ramp up. We monitor the displacement and velocity of the top-end node of the disk in Fig. 8(top). One observes that a steady state is reached after about 40 cycles, with the displacement of -0.5 ± 12.5 nm, and a velocity of 0.05 ± 1.15 m/s.

Case 2: If we now excite the disk at a load $V_{DC} = 6.45$ kV, $V_{AC} = 4.3$ kV and $V_D = 240$ V but with the initial gap to the output electrodes being $g_0 = 9.6$ nm, and the initial gap between the input electrodes and the disk being 6 μm, then as the output electrodes are closer to the disk, the disk impacts the output electrodes after about 5 cycles. In Fig. 8(bottom) we monitor the displacement and velocity of the top-end node of the disk. After 40 cycles, we observe the displacement and velocity reach steady state contact, where the displacement oscillates in $[-11.9, 9.6]$ nm and the velocity in $[-1.1, 1.4]$ m/s. In this example one observes about 15% persistent contact during one loading cycle.

4.3.2 CSS method: Reso-Switch

We now employ Alg. 1 in order to find solutions to (34) directly. As with the FTS solution we employ the explicit time-stepper. We find the initial conditions $\boldsymbol{X}_0$ according to Alg. 1, and then we evolve equations (21) and (22) with these initial conditions over one period T in order to compare the results to the FTS solution. In Fig. 8(column 3), we monitor the top-disk-node displacement and velocity for *Case 1* and *2* respectively. As in the previous example, the direct solution via Alg. 1 shows an equally excellent agreement when compared to the full time-stepping through the transient phase from zero initial conditions. In this plot we have labeled various time-instants $1 - 5$ in the steady state displacement [Fig. 8(third column)], as well as in the phase portrait [Fig. 8(fourth column)]. Note in particular that the CSS algorithm is capable of handling highly nonlinear electro-mechanical impact response at steady state.

Again we have tracked the residual (39) for the transient as well as the CSS solution. In Fig. 9 we plot the residual for *Case 1* in black (no contact), and for *Case 2* in red (contact). We observe a slightly slower convergence for *Case 2*, about 5 additional cycles, to reach a steady contact state during the transient solution when compared to *Case 1*, where no contact occurs [Fig. 9(left)]. This is also observed in Fig. 9(right) for the CSS solution, where convergence is reached after 7 iterations for *Case 2* involving impact, and convergence is reached after 4 iterations for *Case 1* without impact. The
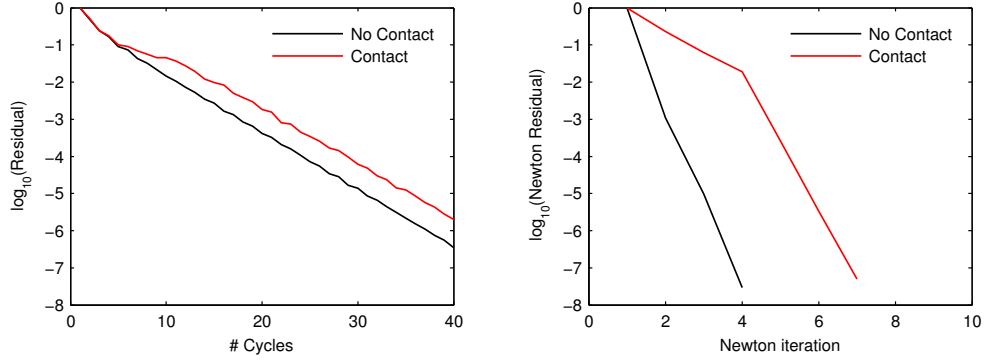
Figure 9: Reso-switch example: convergence of the residual (39) for *Case 1* in black (no contact), and for *Case 2* in red (contact) during (left) the full transient solution from zero initial conditions, and (right) the direct cyclic steady state solution (CSS) via Alg. 1.

observed speed-up in this example is $S = 6.2$ for *Case 1*, and slightly lower $S = 4.1$ for *Case 2*.

Note that for *Case 1* and *2* we have assumed a damping value $\xi = 5.6 \cdot 10^{-2}$. We now test the numerical solutions for $V_{DC} = 6.45$ kV, $V_{AC} = 4.3$ kV, $V_D = 240$ V and the initial gap to the output electrodes $g_0 = 2.2$ μm as in *Case 1*, but with varying damping values $\xi \in \{1.4 \cdot 10^{-2}, 2.8 \cdot 10^{-2}, 5.6 \cdot 10^{-2}, 2.2 \cdot 10^{-1}\}$. As the damping value decreases, we have to adjust the number of time-steps in order to achieve convergence of the residual due to the higher accuracy requirements (see Section 4.1). In this study we have used $2\pi/(\omega \Delta t_n) = 36$ explicit steps per cycle for $\xi = 2.2 \cdot 10^{-1}$, 52 steps per cycle for $\xi = 5.6 \cdot 10^{-2}$, 72 steps per cycle for $\xi = 2.8 \cdot 10^{-2}$, and 104 steps per cycle for $\xi = 1.4 \cdot 10^{-2}$. Typical convergence plots for the FTS solution are shown in Fig. 10(left), and for the CSS solution in Fig. 10(right). Similar observations as with the nanotube vibration example are made: while the transient solution requires significantly more cycles to reach a steady state at lower damping values, the CSS solution is converged within 4 to 5 Newton steps. Thus the observed speed-ups are higher at lower damping values. In accordance with (41) we have measured $S = 3.5$ at $\xi = 2.2 \cdot 10^{-1}$, $S = 6.2$ at $\xi = 5.6 \cdot 10^{-2}$, $S = 11.2$ at $\xi = 2.8 \cdot 10^{-2}$, and $S = 16.7$ at $\xi = 1.4 \cdot 10^{-2}$. We summarize all performance tests done for the reso-switch example, as well as for the nanotube vibration in the next section.
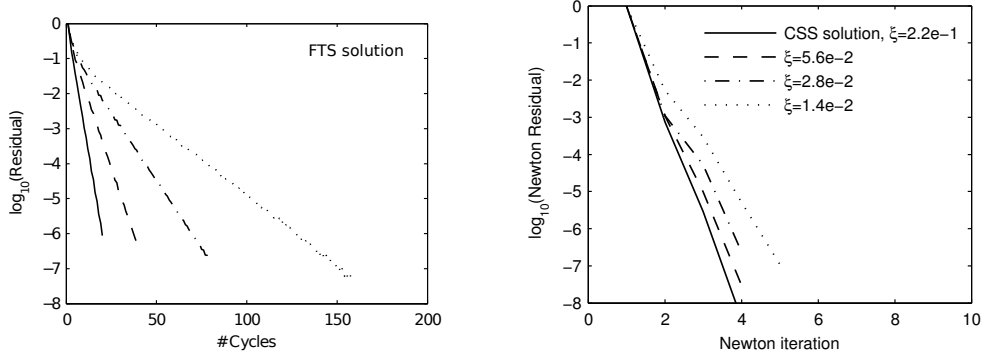
Figure 10: Reso-switch example: (left) convergence of the residual for the transient solution (black) at various damping ratios as indicated in the right figure; (right) convergence of the residual of the direct cyclic steady state solution (CSS) via Alg. 1 for various damping ratios ξ.

4.4 Performance of the GMRES algorithm and Computational Speed-up

As we have noted in the nanotube vibration, as well as the reso-switch example, the measured speed-ups are higher for lower damping values ξ. This is mainly due to the increased number of cycles to reach a steady state for the FTS solution, whereas the Newton algorithm via Alg. 1 has been demonstrated to be relatively unaffected by ξ. In Fig. 11 we plot all speed-ups for the various tests of the nanotube vibration and the reso-switch. We observe power law computational speed-ups of the CSS solution in comparison to a transient solution of the form

$$S = 0.6 \cdot \xi^{-0.8}, \tag{44}$$

where we have measured S according to (41) for the different test cases. As mentioned in Section 3.1, we have investigated two ways to assemble the tangent operator for the direct steady state solution. While the full tangent assembly as in (38) will deliver most accurate results, the use of GMRES will significantly speed-up the calculation during the iterative Newton solution. In accordance with [6], we use the tolerance $||Ax-b||/||b|| < 10^{-3}$ in order to determine the number of Arnoldi iterations for each Newton step. Note that in our examples we observed that the number of Arnoldi iterations increases
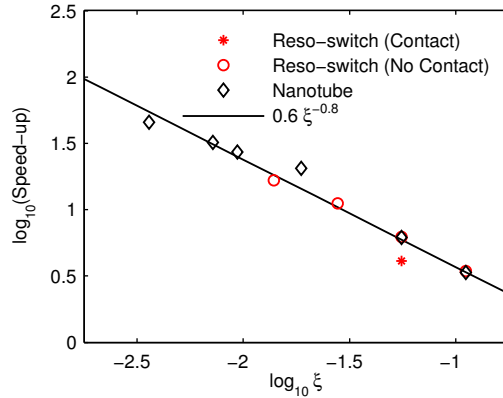
Figure 11: Speed-up of the direct cyclic steady state solution (CSS) via Alg. 1 versus a classical transient time-stepping from zero initial conditions.

for lower damping values (see Tab. 2), and thus the computational speed-up shows only sub-linear growth.

5   Conclusion

We have presented a numerical method to efficiently find the cyclic steady state response of electro-mechanical devices that are excited at resonance. The method features a full-field simulation of the mechanical deformation and the electrical field, incorporating dynamical impact. Whereas the mechanical motion is discretized by a Lagrangian finite element scheme, we employ a fixed grid approach to solve for the electrical field in combination with a higher-order immersed boundary method to track the mechanical motion. This approach reveals several advantages in comparison to traditional Lagrangian or ALE methods – in particular there is no mesh-motion or re-meshing required during large deformations or the closing of gaps during contact. The proposed direct method to solve for cyclic steady states has been demonstrated for two NEMS/MEMS examples, including the vibration of a carbon nanotube at ultra-high frequencies > 1 GHz, and the excitation of a wine-glass disk resonator in forced vibration, as well as in dynamic steady contact. For the presented examples, we show excellent agreement of the direct solution of the cyclic steady state in comparison to the full transient solution from zero initial conditions. The computational speed-up

of the discussed examples scales inversely with the damping ξ according to $S = 0.6 \cdot \xi^{-0.8}$, where we tested $\xi > 10^{-3}$. In the presented examples we have limited ourselves to $\xi > 10^{-3}$ using second order accurate time-integration schemes. For lower damping values ξ, the use of higher-order integration schemes will become necessary to attain accurate results with a reasonable number of time-steps. The development of such higher-order methods must be done within in the context of energy-conserving impact algorithms for the electro-mechanical problem, which is still a subject of current research.

References

[1] Lin Y, Riekkinen T, Li WC, Alon E, Nguyen CC. A Metal Micromechanical Resonant Switch for On-Chip Power Applications. *IEEE IEDM11*, 2011; 497–500.

[2] Jensen K, Weldon J, Garcia H, Zettl A. Nanotube Radio. *Nano Letters* 2007; **7**:3508–3511.

[3] Lin Y, Liu R, Li WC, Akgul M, Nguyen CC. A Micromechanical resonant charge pump. *Solid-State Sensors, Actuators and Microsystems (TRANSDUCERS & EUROSENSORS XXVII)*, Barcelona, Spain, 2013; 1727–1730.

[4] Lin Y, Liu R, Li WC, Nguyen CC. Polycide contact interface to suppress squegging in micromechanical resoswitches. *Micro Electro Mechanical Systems (MEMS), 2014 IEEE 27th International Conference*, San Francisco, CA, 2014; 1273–1276.

[5] Ambrose D, Wilkening J. Computing Time-Periodic Solutions of Nonlinear Systems of Partial Differential Equations. *Proceedings of Hyperbolic Problems: Theory, Numerics, and Applications. Beijing, China, 2010*, Higher Education Press, 2012; 237–280.

[6] Govindjee S, Potter T, Wilkening J. Cyclic steady states of treaded rolling bodies. *International Journal for Numerical Methods in Engineering* 2014; **99**:203–220.

[7] Viswanath D. Recurrent motions within plane Couette turbulence. *Journal of Fluid Mechanics* 2007; **580**:339–358.

[8] Ambrose D, Wilkening J. Computation of time-periodic solutions of the Benjamin-Ono equation. *Journal of Nonlinear Science* 2010; **20**:277–308.

[9] Williams M, Wilkening J, Shlizerman E, Kutz J. Continuation of periodic solutions in the waveguide array mode-locked laser. *Physica D* 2011; **240**:1791–1804.

[10] Wilkening J, Yu J. Overdetermined shooting methods for computing standing water waves with spectral accuracy. *Computational Science & Discovery* 2012; **5**:014 017–1–38.

[11] Brandstetter G, Govindjee S. A high-order immersed boundary discontinuous-Galerkin method for Poisson's equation with discontinuous coefficients and singular sources. *International Journal for Numerical Methods in Engineering* 2015; **101**:847–869.

[12] Brandstetter G, Govindjee S. An Eulerian-Lagrangian finite element method for nonlinear electro-mechanics. *in preparation,* 2016.

[13] Brandstetter G. A High-order Eulerian-Lagrangian Finite Element Method for Coupled Electro-mechanical Systems. *Doctoral Thesis*, University of California, Berkeley, CA, 2015.

[14] Moës N, Dolbow J, Belytschko T. A Finite Element Method for Crack Growth without Remeshing. *International Journal for Numerical Methods in Engineering* 1999; **46**:131–150.

[15] Belytschko T, Black T. Elastic Crack Growth in Finite Elements with Minimal Remeshing. *International Journal for Numerical Methods in Engineering* 1999; **45**:601–620.

[16] Lew A, Buscaglia G. A discontinuous-Galerkin-based immersed boundary method. *International Journal for Numerical Methods in Engineering* 2008; **76**:427–454, doi:10.1002/nme.

[17] Zienkiewicz O, Taylor R, Zhu J. *The Finite Element Method: Its Basis and Fundamentals*. 6 edn., Butterworth-Heinemann: New York, 2005.

[18] Hughes T. *The Finite Element Method: Linear Static and Dynamic Finite Element Analysis*. Prentice-Hall, Inc.: Englewood Cliffs, N.J., 1987.

[19] Belytschko T, Chiapetta R, Bartel H. Efficient large scale non-linear transient analysis by finite elements. *International Journal for Numerical Methods in Engineering* 1976; **10**:579–596.

[20] Knoll D, Keyes D. Jacobian-free Newton-Krylov methods: a survey of approaches and applications. *Journal of Computational Physics* 2004; **193**:357–397.

[21] Iijima S. Helical microtubules of graphitic carbon. *Nature* 1991; **354**:56–58.

[22] Collins P, Zettl A, Bando H, Thess A, Smalley R. Nanotube Nanodevice. *Science* 1997; **278**:100–103.

[23] Weldon J, Alemán B, Sussman A, Gannett W, Zettl A. Sustained mechanical self-oscillations in carbon nanotubes. *Nano Letters* 2010; **10**:1728–1733.

[24] Alemán B, Sussman A, Mickelson W, Zettl A. A Carbon Nanotube-based NEMS Parametric Amplifier for Enhanced Radio Wave Detection and Electronic Signal Amplification. *Journal of Physics: Conference Series* 2011; **302**:012 001–1–6.

[25] Govindjee S, Sackman J. On the use of continuum mechanics to estimate the properties of nanotubes. *Solid State Communications* 1999; **110**:227–230.

[26] Saffar K, Jamilpour N, Najafi A, Rouhi G, Arshi A, Fereidoon A. A Finite Element Model for estimating Young's Modulus of Carbon Nanotube Reinforced Composites Incorporating Elastic Cross-Links. *World Academy of Science, Engineering and Technology* 2008; **47**:219–222.

[27] Kis A, Zettl A. Nanomechanics of carbon nanotubes. *Philosophical Transactions of the Royal Society A* 2008; **366**:1591–1611.

[28] Jensen K, Peng H, Zettl A. Limits of Nanomechanical Resonators. *Nanoscience and Nanotechnology*, 2006; 06EX411C–68–71.

[29] Armero F. Assumed Strain Finite Element Methods. *Finite Element Methods: 1970's and Beyond, (Eds.) Franca, L.P., Tezduyar, T.E., Masud, A., CIMNE, Barcelona, Spain*, 2004; 46–61.

[30] Abdelmoneum M, Wang J, Demirci M, Nguyen CC. Stemless wine-glass-mode disk micromechanical resonators. *Proceedings, 16th Int. IEEE Micro Mechanical Systems Conf., Kyoto, Japan*, 2003; 698–701.

[31] Lin Y, Li WC, Ren Z, Nguyen CC. The micromechanical resonant switch ("Resoswitch"). *Tech. Digest, 2008 Solid-State Sensor, Actuator, and Microsystems Workshop, Hilton Head, South Carolina*, 2008; 40–43.

[32] Demmel J. *Applied Numerical Linear Algebra*. SIAM Society for Industrial and Applied Mathematics: Philadelphia, 1997.